

A Multicenter Benchmark of Multiple Instance Learning Models for Lymphoma Subtyping from HE-stained Whole Slide Images

Rao Muhammad Umer ¹

UMER.RAO@HELMHOLTZ-MUNICH.DE

Daniel Sens ¹

DANIEL.SENS@HELMHOLTZ-MUNICH.DE

Jonathan Noll ¹

JONATHAN.NOLL.LEON@GMAIL.COM

Sohom Dey ¹

SOHOM21D@GMAIL.COM

Christian Matek ^{1,2,7}

CHRISTIAN.MATEK@UK-ERLANGEN.DE

Lukas Wolfseher ⁸

LUKAS.WOLFSEHER@INFORMATIK.UNI-KIEL.DE

Rainer Spang ⁸

RAINER.SPANG@KLINIK.UNI-R.DE

Ralf Huss ⁹

HUSS@BIO-M.ORG

Johannes Raffler ⁹

JOHANNES.RAFFLER@UK-AUGSBURG.DE

Sarah Reinke ¹⁰

SREINKE@PATH.UNI-KIEL.DE

Ario Sadafi ^{1,6}

ARIO.SADAFI@HELMHOLTZ-MUNICH.DE

Wolfram Klapper ¹⁰

WKLAPPER@PATH.UNI-KIEL.DE

Katja Steiger ⁶

KATJA.STEIGER@TUM.DE

Kristina Schwamborn ⁶

KSCHWAMBORN@TUM.DE

Carsten Marr ^{1,2,3,4,5}

CARSTEN.MARR@HELMHOLTZ-MUNICH.DE

¹ *Institute of AI for Health, Helmholtz Munich, Munich, Germany*

² *Department of Medicine III, Ludwig-Maximilian-University Hospital, Munich, Germany*

³ *Computational Health Center & Helmholtz AI, Helmholtz Munich, Neuherberg, Germany*

⁴ *German Cancer Consortium (DKTK), partner site Munich, Germany*

⁵ *Munich Center for Machine Learning (MCML), Munich, Germany*

⁶ *Technical University of Munich, Munich, Germany*

⁷ *Institute of Pathology, Erlangen, Germany*

⁸ *University of Kiel, Kiel, Germany*

⁹ *Institute for Digital Medicine, University Hospital, Augsburg, Germany*

¹⁰ *Institute of Pathology, University Hospital, Kiel, Germany*

Editors: Under Review for MIDL 2025

Abstract

Timely and accurate lymphoma diagnosis is essential for guiding cancer treatment. Standard diagnostic practice combines hematoxylin and eosin (HE)-stained whole slide images with immunohistochemistry, flow cytometry, and molecular genetic tests to determine lymphoma subtypes, a process requiring costly equipment, skilled personnel, and causing treatment delays. Deep learning methods could assist pathologists by extracting diagnostic information from routinely available HE-stained slides, yet comprehensive benchmarks for lymphoma subtyping on multicenter data are lacking.

In this work, we present the first multicenter lymphoma benchmarking dataset covering four common lymphoma subtypes and healthy control tissue. We systematically evaluate five publicly available pathology foundation models (H-optimus-1, H0-mini, Virchow2,

UNI2, Titan) combined with attention-based (AB-MIL) and transformer-based (TransMIL) multiple instance learning aggregators across three magnifications ($10\times$, $20\times$, $40\times$). On in-distribution test sets, models achieve multiclass balanced accuracies exceeding 80% across all magnifications, with all foundation models performing similarly and both aggregation methods showing comparable results. The magnification study reveals that $40\times$ resolution is sufficient, with no performance gains from higher resolutions or cross-magnification aggregation. However, on out-of-distribution test sets, performance drops substantially to around 60%, highlighting significant generalization challenges. To advance the field, larger multicenter studies covering additional rare lymphoma subtypes are needed. We provide an automated benchmarking pipeline to facilitate such future research.

Keywords: Multicenter Lymphoma Benchmark, Multiple Instance Learning, Whole Slide Images, Pathology Foundation Models.

1. Introduction

Cancer is one of the deadliest diseases and remains an insurmountable obstacle to advance the quality and expectancy of life all over the world (Bray et al., 2021). Lymphoma is a type of blood cancer that originates in the lymphatic system, which is a critical part of human body’s immune system. It specifically arises from lymphocytes, white blood cells that play a key role in defending the body against infections. Lymphomas are broadly classified into two main categories (Lewis et al., 2020): Hodgkin lymphoma (HL) and non-Hodgkin lymphoma (NHL), with each category having numerous subtypes. The diagnosis of lymphoma involves a combination of clinical evaluation, medical imaging, and most importantly, biopsy of the affected tissue. The biopsy is examined under a microscope (i.e., digitized as gigapixel HE (Hematoxylin and Eosin) stained whole slide images), and additional tests like immunohistochemical (IHC) stains, flow cytometry, cytogenetic, and molecular analysis help to determine the specific subtype of lymphoma (Lewis et al., 2020). These auxiliary tests require costly equipment, expensive reagents, and trained personnel. Treatment varies depending on the lymphoma subtype, stage, and other factors such as the patient’s overall health. Common treatment options (Lewis et al., 2020) include chemotherapy, radiation therapy, targeted therapy, immunotherapy, and stem cell transplantation.

Histopathology plays a central role in clinical medicine for tissue-based diagnostics and in biomedical research as a basis for understanding cellular and molecular mechanisms of disease by microscopic evaluation of morphological changes (Campanella et al., 2023). Advances in histology slide scanning enable the digitization of entire histology slides into a whole slide image (WSI), paving the way for computer-aided diagnosis. In contrast to IHC, flow cytometry, and molecular genetic tests, HE-stained WSIs are inexpensive and widely available. Recent studies (Vorontsov et al., 2024; Zimmermann et al., 2024; Chen et al., 2024b; Bioptimus, 2025; Ding et al., 2025; Filiot et al., 2025) have shown rapid progress in pathology foundation models (FMs) on diverse large unlabeled WSI datasets. These models learn transferable representations that can be adapted to a wide range of downstream pathology tasks with relatively less annotated data. Among the most prominent pathology FMs are: Virchow2 (Zimmermann et al., 2024), UNI2 (Chen et al., 2024b), H-optimus-1 (Bioptimus, 2025), Titan (Ding et al., 2025), and H0-mini (Filiot et al., 2025). For downstream pathology tasks, Multiple Instance Learning (MIL) has been applied as a key methodology in computational pathology (Ilse et al., 2018; Campanella et al., 2019;

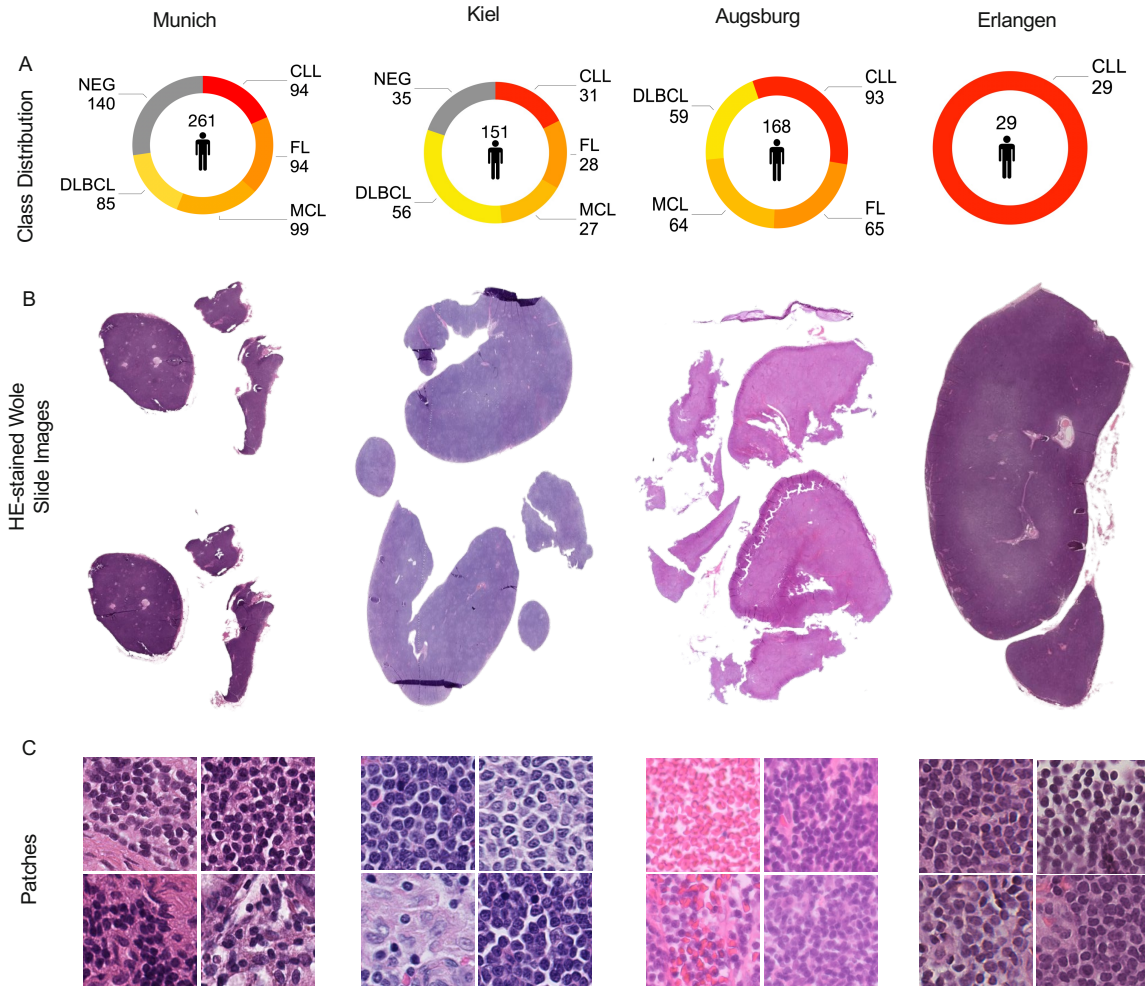


Figure 1: A: Our multicenter lymphoma benchmark datasets comprises 5 classes : Follicular Lymphoma (FL), Chronic Lymphocytic Leukemia (CLL), Mantle Cell Lymphoma (MCL), Diffuse Large B-Cell Lymphoma (DLBCL) and healthy controls (NEG), with total 999 HE WSIs from 609 individual patients. The total number of WSIs in each class are given. B: Thumbnails of exemplary CLL WSIs. C: Random patches of 256×256 pixels at $40\times$ magnification.

Sadafi et al., 2020; Shao et al., 2021), where labels are assigned at the “bag” level (WSI), while learning is performed from individual instances (patches) within each bag. MIL is particularly well-suited for histopathology, where detailed annotations are often difficult to obtain.

Earlier studies (Vrabac et al., 2021; Orlov et al., 2010; Vorontsov et al., 2024) have demonstrated strong performance in distinguishing a limited set of lymphoma types, such as Diffuse Large B-Cell Lymphoma (DLBCL) and Follicular Lymphoma (FL) from HE-

stained WSI. Their clinical utility remains limited due to narrow subtype coverage. In this work, we present first multicenter lymphoma benchmark covering four common subtypes simultaneously in Europe and healthy control tissue (Figure 1). Moreover, we provide an automated benchmarking MIL pipeline for external evaluation (Figure 2). Our main contributions are the following:

- We present a first multicenter lymphoma benchmark for the four most frequent subtypes and healthy controls.
- We provide a deep multiple instance learning pipeline with five publicly available pathology foundation models for validation studies.
- We evaluate attention-based MIL models on in-distribution and out-of-distribution lymphoma datasets at three different resolutions.

2. Methodology

The deep learning pipeline for our experiments consists of lymphoma whole slide imaging, tissue segmentation and patch extraction, feature extraction, and lymphoma subtype classification (Figure 2). In the following, we describe each component in detail.

2.1. Lymphoma subtypes

Figure 1 shows the data used in our experiments. The lymphoma subtypes in the datasets are Chronic Lymphocytic Leukemia (CLL), Follicular Lymphoma (FL), Mantle Cell Lymphoma (MCL), and Diffuse Large B-Cell Lymphoma (DLBCL). In addition, the dataset contains WSIs showing only healthy tissue sections, which are used as a control class and designated as negative (NEG). CLL is a B-cell neoplasm that originates in the bone marrow and is characterized by the progressive accumulation of mature-appearing lymphocytes, which expand into the peripheral blood and infiltrate lymphoid organs, ultimately impairing normal organ function (Ghia et al., 2007). FL arises from germinal-center B-cells—centrocytes and centroblasts that proliferate aberrantly and form characteristic follicular or follicle-like structures (Xerri et al., 2016). MCL develops from mantle-zone B-cells and typically presents with generalized lymphadenopathy or splenomegaly; it is defined by the expansion of cyclin-D1-driven malignant lymphocytes and displays an aggressive clinical course (Schieber et al., 2018). DLBCL represents a high-grade B-cell lymphoma in which antibody-producing lymphocytes undergo malignant transformation, leading to rapidly enlarging masses in lymph nodes or extranodal sites due to uncontrolled proliferation (Morton et al., 2006). Figure 3 shows the morphology of the four lymphoma classes in the Munich dataset.

2.1.1. MUNICH

Histology slides have been selected from the archive of the Institute of Pathology, Technical University of Munich, Germany. The dataset consists of 513 HE-stained WSIs obtained

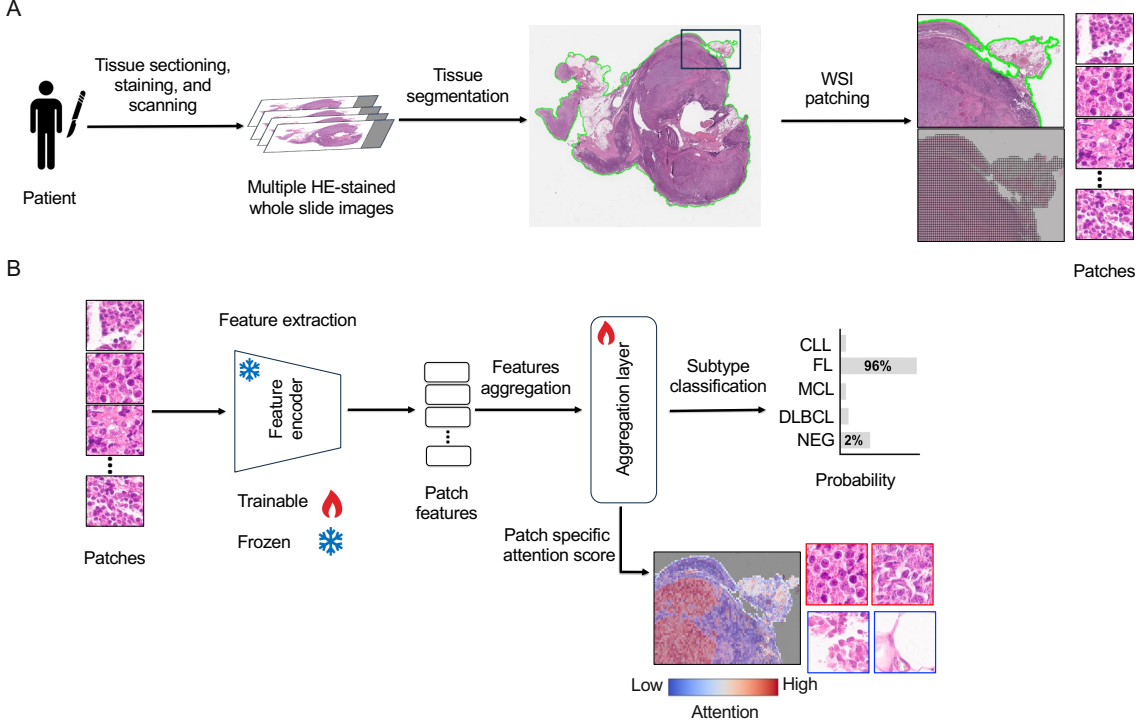


Figure 2: A deep multiple instance learning pipeline from whole slide images acquisition to interpretability. A: Multiple whole slide images (WSIs) are obtained per patient after tissue sectioning, HE staining, and digital scanning. Thousand of the patches are extracted from each WSI by segmenting the tissue regions. B: The extracted patches are passed to a pretrained Encoder model (frozen) to extract feature vectors. The stacked feature vectors are fed to attention based aggregation layer (trainable) to aggregate patch-level information into slide-level representations, which are used to make the final lymphoma subtyping prediction. In addition, for each subtype, we extract attention scores to visualize important regions of the WSI.

from 261 patients containing tissue segments from lymph node biopsies. The WSIs were scanned at $40\times$ magnification with Aperio AT2 scanner.

The subtypes in the dataset are: FL, CLL, MCL, DLBCL, and NEG (see Figure 1).

2.1.2. KIEL

Histology slides were selected from the archive of the Institute of Pathology, University Hospital, Kiel, Germany. The dataset consists of 177 HE-stained WSIs obtained from lymphoid tissue specimens of 151 patients. The WSIs were scanned at $40\times$ magnification with Hamamatsu scanner. It includes FL, CLL, MCL, DLBCL, and NEG. Some whole slides in

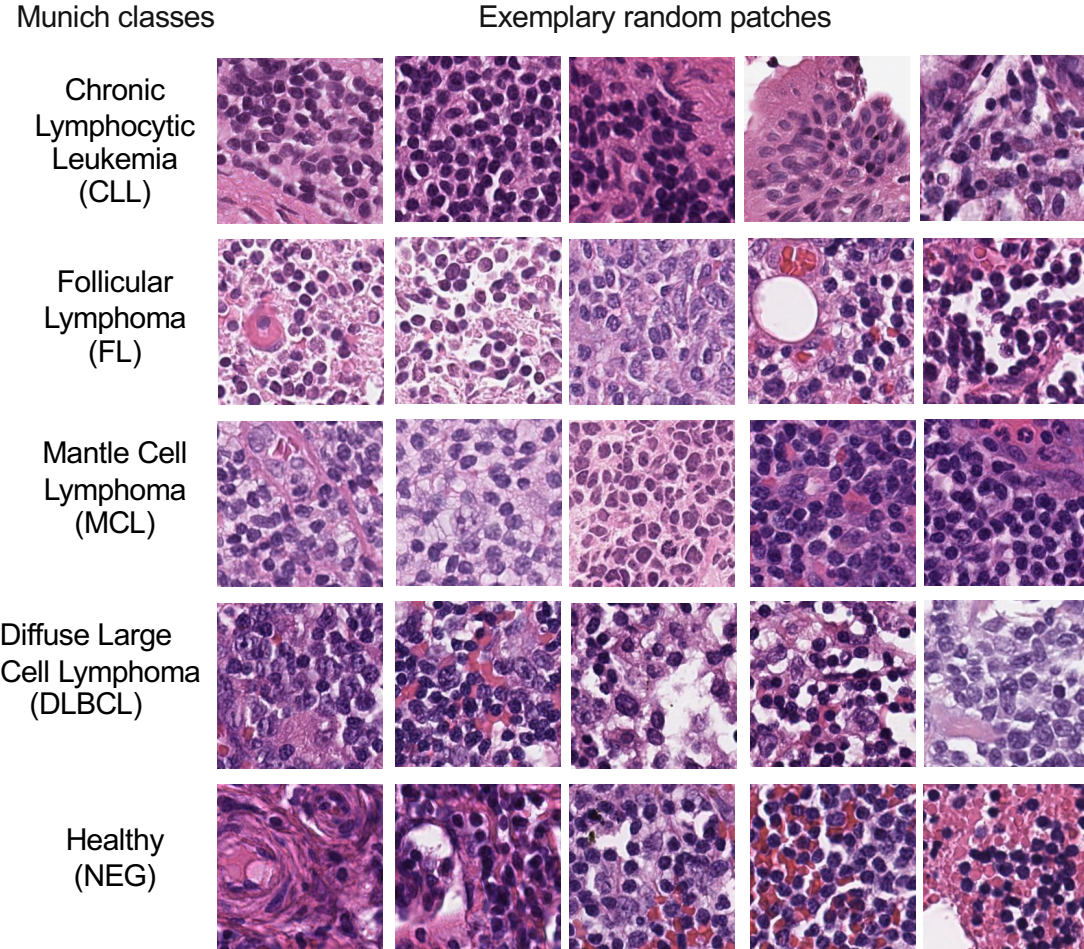


Figure 3: Five lymphoma classes morphology overview in Munich dataset. Five randomly selected patches from a heterogenous WSI of each class at a size of 256×256 pixels with a magnification of $40\times$, at which individual cells become recognisable.

the dataset originate from the same patient, as these represent the same biopsy scanned twice rather than a different section. Although the scans may exhibit slight color variations, their overall appearance remains largely similar (see Figure 1).

2.1.3. AUGSBURG

Histology slides were selected from the archive of the University Hospital, Augsburg, Germany. The dataset consists of de-identified 290 HE-stained and immunohistochemistry (IHC) stained WSIs obtained from 168 patients. The WSIs were scanned at $40\times$ magnification with Philips scanner. The subtypes in the dataset are: FL, CLL, MCL, and DLBCL. The class labels were manually derived from the reports by the pathology's quality expert

(see Figure 1).

2.1.4. ERLANGEN

Histology slides were selected from the archive of the Institute of Pathology, University Hospital, Erlangen, Germany. The dataset consists of de-identified 29 HE-stained WSIs obtained from 29 patients. The WSIs were scanned at $40\times$ magnification. It includes only CLL class (see Figure 1).

2.2. Tissue segmentation and patch extraction

Tissue segmentation filters out background areas in WSIs, reducing the number of irrelevant patches and speeding up non-overlapping patch extraction. Traditional techniques typically rely on image-processing heuristics such as binary or Otsu thresholding, which require manual parameter tuning and often fail to generalize across stains. These approaches also struggle to distinguish true tissue from common artifacts, including pen marks and bubbles. Trident (Zhang et al., 2025) is a recent alternative for robust and stain-agnostic tissue segmentation and patch extraction. After tissue segmentation, the patching step divides the tissue-containing regions into N non-overlap image patches with a size of 256×256 pixel at specific magnification for later processing by a feature encoder (Figure 2A). We can represent the resulting patches as $\mathbf{X} = \{\mathbf{x}_1, \dots, \mathbf{x}_N\}, \mathbf{x}_i \in [0, 255]^{256 \times 256 \times 3}$, where \mathbf{X} is called a bag for a WSI, and \mathbf{x}_i is called the i -th instance.

2.3. Feature extraction

Due to the high dimensionality of a WSI, \mathbf{X} usually consists of a large number of instances and cannot be processed by the downstream aggregation models. Thus, we first pass patches to a pretrained encoder to yield patch features by compressing the high dimensional visual information into a one dimensional feature vector. Lets suppose f_ψ is a pretrained encoder with parameters ψ , for each patch $\mathbf{x}_i \in \mathbf{X}$ the corresponding feature vector is obtained as $\mathbf{h}_i = f_\psi(\mathbf{x}_i)$. The WSI is represented by a bag of instance features $\mathbf{H} = \{\mathbf{h}_1, \dots, \mathbf{h}_N\}$, which is passed as an input to the aggregation layer (see Figure 2B). In our pipeline, the pretrained encoders can either be used to extract patch-level or slide-level features.

2.4. Lymphoma subtype classification

We use the deep multiple instance learning (MIL) framework for the trainable aggregation layer to classify the bag \mathbf{H} of instance features into the five classes of our lymphoma dataset. The aggregation layer takes as input a bag \mathbf{H} of N instance features and outputs a patient latent vector $\mathbf{z} = \sum_{k=1}^N a_k \mathbf{h}_k$, where a_k is the attention score.

Finally, the patient latent vector \mathbf{z} is passed to classifier to obtain predicted class scores $\hat{\mathbf{Y}}$. During training, the cross-entropy loss is computed between the predicted WSI class label $\hat{\mathbf{Y}}$ and ground-truth label $\mathbf{Y} \in \{1, \dots, C\}$.

3. Experimental Results

3.1. Preprocessing

Our HE-stained WSIs contain pen marks and artifacts, i.e., blurring, compression, water bubbles. In our pipeline, we use Trident (Zhang et al., 2025) for both tissue segmentation and patch extraction; it employs a DeepLabV3-based segmentation model that provides more robust and stain-agnostic tissue detection and segmentation, and further extract non-overlapping patches from a WSI.

3.2. Evaluation

We split the patient-wise for five-fold cross-validation with train, validation, and test sets with a ratio of 80%, 10%, and 10%, respectively, to assess the performance of trained MIL models. To prevent data leakage and overfitting, all images of one patient are assigned to the same fold. The training set is shuffled to introduce slight variability, while the validation and test sets remain unshuffled to ensure consistent and reliable evaluation.

The model’s performance is evaluated using the Area Under the ROC Curve (AUC), Macro F1-score, and Balanced Accuracy (BACC) metrics. These metrics are calculated on both the validation and test datasets to provide a comprehensive assessment of classification effectiveness. Additionally, confusion matrices are analyzed to interpret the distribution of prediction errors.

3.3. Implementation details

We use several pretrained vision encoders for feature extraction, ResNet50 (baseline) (He et al., 2016), H-optimus-1 (Bioptimus, 2025), H0-mini (Filiot et al., 2025), Virchow2 (Zimmermann et al., 2024), UNI2 (Chen et al., 2024a), Titan (Ding et al., 2025). Each model independently process the WSI patches, generating s-dimensional embeddings encoding the visual representation of each WSI.

The MIL models are trained under a weakly supervised learning setting, as only slide-level labels are available and no detailed annotations for individual patches. We use the MIL architecture, employing three variants: attention-based deep MIL (AB-MIL) (Ilse et al., 2018), transformer-based MIL (TransMIL) (Shao et al., 2021), and TransMIL + BEL (Sens et al., 2023). These models aggregate features extracted from individual instances (patches) within each WSI to generate a single, comprehensive representation of the entire slide. By learning to assign different weights to instances, the architectures can capture the most relevant morphological features contributing to the classification task. We address class imbalance by applying balanced sampling at the patient level during aggregator model training, rather than relying on slide-level label balancing. This strategy mitigates subtype imbalance effects and ensures that model performance is not biased by overrepresented classes.

The MIL models are trained for 50 epochs. Each training step involves a forward pass to generate predictions, computation of the cross-entropy loss by comparing predictions with ground-truth slide-level labels, and parameter updates via backpropagation using the AdamW optimizer, which combines weight decay with adaptive learning rate adjustments. To support convergence, a learning rate schedule with a warm-up phase of 10 epochs is used,

Table 1: **Magnification study**: Five-fold cross-validation results for lymphoma subtype classification on Munich dataset at different magnification level, $40\times$, $20\times$, and $10\times$. Performance is reported in terms of Area Under ROC (AUC), Macro F1-score, and balanced accuracy (BACC).

Magnification	Encoder	Embedding Dim	Aggregator	AUC	F1-score	BACC
$40\times$	ResNet50 (Baseline)	1024	AB-MIL	0.89 ± 0.03	0.66 ± 0.06	0.67 ± 0.06
			TransMIL	0.85 ± 0.02	0.58 ± 0.02	0.59 ± 0.03
			TransMIL + BEL	0.87 ± 0.02	0.62 ± 0.04	0.63 ± 0.03
	UNI2 (Patch-level)	1536	AB-MIL	0.95 ± 0.01	0.79 ± 0.02	0.79 ± 0.03
			TransMIL	0.94 ± 0.01	0.75 ± 0.04	0.75 ± 0.04
			TransMIL + BEL	0.96 ± 0.01	0.80 ± 0.03	0.80 ± 0.03
	Titan (Slide-level)	768	Linear	0.95 ± 0.01	0.78 ± 0.02	0.78 ± 0.01
			AB-MIL	0.96 ± 0.01	0.83 ± 0.06	0.82 ± 0.05
			TransMIL	0.96 ± 0.01	0.82 ± 0.03	0.82 ± 0.03
			TransMIL + BEL	0.96 ± 0.01	0.82 ± 0.04	0.81 ± 0.04
$20\times$	ResNet50 (Baseline)	1024	AB-MIL	0.89 ± 0.02	0.63 ± 0.04	0.64 ± 0.04
			TransMIL	0.81 ± 0.04	0.50 ± 0.04	0.51 ± 0.04
			TransMIL + BEL	0.84 ± 0.02	0.58 ± 0.02	0.58 ± 0.03
	UNI2 (Patch-level)	1536	AB-MIL	0.95 ± 0.02	0.77 ± 0.03	0.77 ± 0.03
			TransMIL	0.94 ± 0.01	0.79 ± 0.04	0.79 ± 0.04
			TransMIL + BEL	0.96 ± 0.01	0.83 ± 0.03	0.83 ± 0.03
	Titan (Slide-level)	768	Linear	0.95 ± 0.01	0.77 ± 0.02	0.77 ± 0.02
			AB-MIL	0.96 ± 0.01	0.82 ± 0.06	0.81 ± 0.07
			TransMIL	0.96 ± 0.01	0.82 ± 0.04	0.82 ± 0.04
			TransMIL + BEL	0.96 ± 0.01	0.82 ± 0.03	0.82 ± 0.04
$10\times$	ResNet50 (Baseline)	1024	AB-MIL	0.85 ± 0.02	0.60 ± 0.07	0.61 ± 0.06
			TransMIL	0.83 ± 0.04	0.52 ± 0.06	0.54 ± 0.06
			TransMIL + BEL	0.82 ± 0.04	0.51 ± 0.04	0.53 ± 0.04
	UNI2 (Patch-level)	1536	AB-MIL	0.95 ± 0.01	0.80 ± 0.04	0.80 ± 0.04
			TransMIL	0.95 ± 0.01	0.80 ± 0.04	0.80 ± 0.04
			TransMIL + BEL	0.96 ± 0.02	0.81 ± 0.05	0.81 ± 0.05
	Titan (Slide-level)	768	Linear	0.94 ± 0.01	0.75 ± 0.04	0.75 ± 0.04
			AB-MIL	0.95 ± 0.02	0.79 ± 0.04	0.79 ± 0.04
			TransMIL	0.94 ± 0.01	0.77 ± 0.04	0.78 ± 0.04
			TransMIL + BEL	0.95 ± 0.01	0.80 ± 0.04	0.80 ± 0.04

linearly increasing the learning rate from 0 to 0.0001. After the warm-up, a cosine decay scheduler gradually reduces the learning rate down to 1e-6. Simultaneously, the weight decay, initially set to 0.04, are gradually increased up to 0.4. A momentum factor of 0.9 is also applied to accelerate optimization.

3.4. Quantitative results

For lymphoma subtype prediction, we assessed model performance across varying magnifications, multiple patch-level and slide-level feature encoders, and both in-distribution and out-of-distribution (OOD) test sets. Our lymphoma subtyping findings should be inter-

Table 2: **Comparison of publicly available feature encoders:** Five-fold cross-validation results for lymphoma subtype classification on Munich and Kiel lymphoma datasets at 40x magnification. Performance is reported in terms of AUC, F1-score, and balanced accuracy (BACC).

Dataset	Encoder	Embedding Dim	Aggregator	IID Test		
				AUC	F1-score	BACC
Munich	ResNet50	1024	AB-MIL	0.89 ±0.03	0.66 ±0.06	0.67 ±0.06
	H-optimus-1	1536		0.96 ±0.01	0.79 ±0.03	0.79 ±0.03
	H0-mini	1536		0.95 ±0.01	0.79 ±0.02	0.78 ±0.01
	Virchow2	2560		0.96 ±0.01	0.77 ±0.04	0.77 ±0.04
	UNI2	1536		0.95 ±0.01	0.79 ±0.02	0.79 ±0.03
	Titan	768		0.96 ±0.01	0.83 ±0.06	0.82 ±0.05
Kiel	ResNet50	1024	AB-MIL	0.85 ±0.05	0.64 ±0.08	0.65 ±0.04
	H-optimus-1	1536		0.97 ±0.01	0.81 ±0.09	0.81 ±0.09
	H0-mini	1536		0.92 ±0.05	0.66 ±0.15	0.69 ±0.13
	Virchow2	2560		0.96 ±0.02	0.72 ±0.11	0.74 ±0.09
	UNI2	1536		0.96 ±0.03	0.82 ±0.07	0.82 ±0.06
	Titan	768		0.96 ±0.02	0.83 ±0.06	0.81 ±0.05

preted as complementary to the “all-task” benchmark (Bareja et al., 2025) rather than directly comparable.

Magnification study (Table 1): On the in-distribution Munich test set, we compared baseline ResNet50, the patch-level encoder UNI2, and the slide-level encoder Titan across 40×, 20×, and 10× magnifications. TransMIL combined with UNI2 or Titan is better than AB-MIL at 40× and 20×, with a slight performance decline observed at 10×. Despite this, AB-MIL remained the most computationally efficient option for training and inference compared to transformer-based MIL methods. TransMIL + BEL show only minimal gains over TransMIL. This behavior is likely due to a mismatch between the BEL objective and the morphological characteristics of lymphoma WSIs: While BEL is designed to regularize bag-level embeddings in transformer-based MIL, lymphoma subtyping relies on heterogeneous and spatially dispersed patterns rather than a single dominant bag embedding. We believe that TransMIL already captures the discriminative context in the slides, leaving limited room for additional gains from BEL. We trained TransMIL + BEL using the original hyperparameters proposed by (Sens et al., 2023), but checked that further parameter tuning did not lead to improvements.

Comparison of publicly available feature encoders (Table 2): Using AB-MIL, we evaluated several open-source pathology feature encoders on the Munich and Kiel in-distribution cohorts. UNI2 and Titan achieved superior performance across both datasets, indicating their strong representation capacity for lymphoma subtyping.

Out-of-distribution generalization (Table 3): Models trained on the Munich dataset using UNI2 or Titan features were evaluated on three external cohorts: Kiel, Augsburg, and Erlangen.

Table 3: **Out-of-distribution generalization:** Five-fold cross-validation results for lymphoma subtype classification on external datasets at $40\times$ magnification. UNI2 and Titan are used as feature encoders and pretrained aggregators (AB-MIL and TransMIL) on Munich dataset. Performance is reported in terms of AUC, F1-score, and balanced accuracy (BACC).

Encoder	OOD Dataset	Aggregator	OOD Test		
			AUC	F1-score	BACC
UNI2	Kiel	AB-MIL	0.88 ± 0.05	0.61 ± 0.06	0.62 ± 0.04
		TransMIL	0.86 ± 0.06	0.58 ± 0.06	0.60 ± 0.04
	Augsburg	AB-MIL	0.82 ± 0.04	0.58 ± 0.05	0.60 ± 0.06
		TransMIL	0.77 ± 0.05	0.50 ± 0.05	0.51 ± 0.05
	Erlangen	AB-MIL	0.75 ± 0.05	0.37 ± 0.07	0.59 ± 0.18
		TransMIL	0.90 ± 0.05	0.75 ± 0.35	0.83 ± 0.24
Titan	Kiel	AB-MIL	0.88 ± 0.05	0.43 ± 0.08	0.48 ± 0.08
		TransMIL	0.84 ± 0.04	0.45 ± 0.10	0.50 ± 0.08
	Augsburg	AB-MIL	0.80 ± 0.03	0.41 ± 0.06	0.48 ± 0.04
		TransMIL	0.77 ± 0.03	0.37 ± 0.06	0.46 ± 0.04
	Erlangen	AB-MIL	0.78 ± 0.05	0.35 ± 0.09	0.53 ± 0.20
		TransMIL	0.86 ± 0.05	0.60 ± 0.25	0.72 ± 0.18

UNI2 paired with AB-MIL achieved the best overall performance on OOD Kiel. The superior performance of UNI2 + AB-MIL on the OOD Kiel cohort is primarily attributable to UNI2’s stronger patch-level representations for cross-domain generalization. UNI2 is trained on large-scale, diverse histopathology datasets and preserves fine-grained cellular morphology, which is critical for lymphoma subtyping. In contrast, Titan operates at the slide level by aggressively reducing token resolution, which improves efficiency but limits its ability to capture subtle, spatially localized lymphoma patterns under domain shift. As a result, UNI2 features generalize more robustly to unseen centers.

UNI2 paired with AB-MIL achieved the best overall performance on OOD Augsburg. We use Augsburg data to assess model robustness under domain shift. To address the label-space mismatch, we report four-class metrics using the original predictions, considering the top-2 class for the those cases where NEG is the top-1 prediction, resulting in comparable performance of our models on the Augsburg dataset.

For the Erlangen dataset, which contains only CLL cases, UNI2 combined with TransMIL yielded the highest accuracy. In the Erlangen cohort, the high standard deviation observed is primarily due to its very small sample size (29 WSIs) and its single-class composition (CLL only). In this setting, balanced accuracy becomes highly sensitive to fold-level variations, leading to inflated variance. Additionally, Erlangen data were acquired using a different scanner, further amplifying instability. We report these results transparently to highlight the challenges of evaluating OOD performance on small, single-class cohorts, rather than as evidence of reliable generalization. Across all OOD evaluations, UNI2 + AB-MIL demonstrated the most robust and stable generalization behavior.

		Munich					Kiel				
		CLL	FL	MCL	DLBCL	NEG	CLL	FL	MCL	DLBCL	NEG
True class	CLL	77	4	5	4	4	22	5	0	1	3
	FL	3	59	18	8	6	1	17	6	2	2
	MCL	4	7	79	4	5	9	5	11	0	2
	DLBCL	4	8	6	62	5	1	2	3	50	0
	NEG	1	0	3	0	136	3	13	0	3	16
		CLL	FL	MCL	DLBCL	NEG	CLL	FL	MCL	DLBCL	NEG

Figure 4: **Confusion matrix comparison on in-distribution Munich and out-of-distribution testsets:** IID testset, Munich, and external OOD test: Kiel, Augsburg, and Erlangen. The MIL models perform strongest on Munich, and better results on Kiel, Augsburg, and Erlangen.

Confusion matrix comparison on in-distribution and out-of-distribution testsets: Figure 4 presents confusion matrices for UNI2 + AB-MIL on the in-distribution Munich test set and the three OOD cohorts. The model performed strongest on the IID Munich dataset, followed by solid results on Kiel, Augsburg, and Erlangen.

Computational efficiency: Table 4 compares computational efficiency of the five pathology foundation models, reporting parameters, FLOPs, and throughput (images per second) measured on a consumer-grade RTX 3090 GPU. For the patch-level FMs, throughput is computed in FP16 precision with a batch size of 32, and we report the mean and

Table 4: **Computational efficiency** statistics of five pathology foundation models, including parameter count, FLOPs, and inference time per image or per slide. Throughput is computed on images per second for patch-level models, and slides per second for slide-level model (Titan).

Model	Params.	FLOPs	Throughput
	[M] (↓)	[G] (↓)	[img or slide/s] (↑)
H-optimus-1	1,135	591.81	82.5 ±4.3
H0-mini	87	44.60	885.1 ±7.1
Virchow2	632	329.11	134.3 ±7.9
UNI2	681	360.71	134.6 ±7.6
Titan	85	36.76	43.95 ±2.3

standard deviation over 500 batches. In whole slide image analysis, where thousands of image patches are encoded for a slide level prediction, this efficiency translates into total processing time with varying number of image patches per slide. For slide-level FMs such as Titan, it operates at the whole slide level by substantially reducing the number of processed tokens during inference. The throughput is computed as slides per second with 10,000 patches per slide on A100 GPU.

3.5. Whole slide image attention visualization

The attention scores can be visualized as heatmaps to highlight diagnostically informative regions, areas assigned high attention, while de-emphasizing regions of low relevance, such as normal tissue or background artifacts. To interpret the spatial distribution of model attention across a WSI, we convert the attention scores corresponding to the predicted class into percentiles and map these normalized values back to their original coordinates on the slide. Fine-grained heatmaps are produced by extracting overlapping patches and averaging the attention values within the overlapping areas. In our workflow, we employ Trident (Zhang et al., 2025) to generate WSI-level attention visualizations (Figure 5 and Figure 7) and to display the patches with the highest attention scores. In Figure 6, UNI2 features generalize more robustly than Titan, and avoid artifact patches. We note that a high-attention score in CLL is given to non-lymphoma areas and in DLBCL to poorly preserved areas (Figure 5). This behavior might be avoidable when training the algorithm with more classes.

4. Limitations

Although this multicenter benchmark is comprehensive, several limitations remain. First, the substantial decrease in performance (20%) on external test sets highlights unresolved out-of-distribution generalization challenges. Scanner-specific color variation, staining differences, and shifts in patient cohorts across clinical sites continue to affect model robustness, as reflected by the performance drop on OOD cohorts. Second, some cohorts exhibit

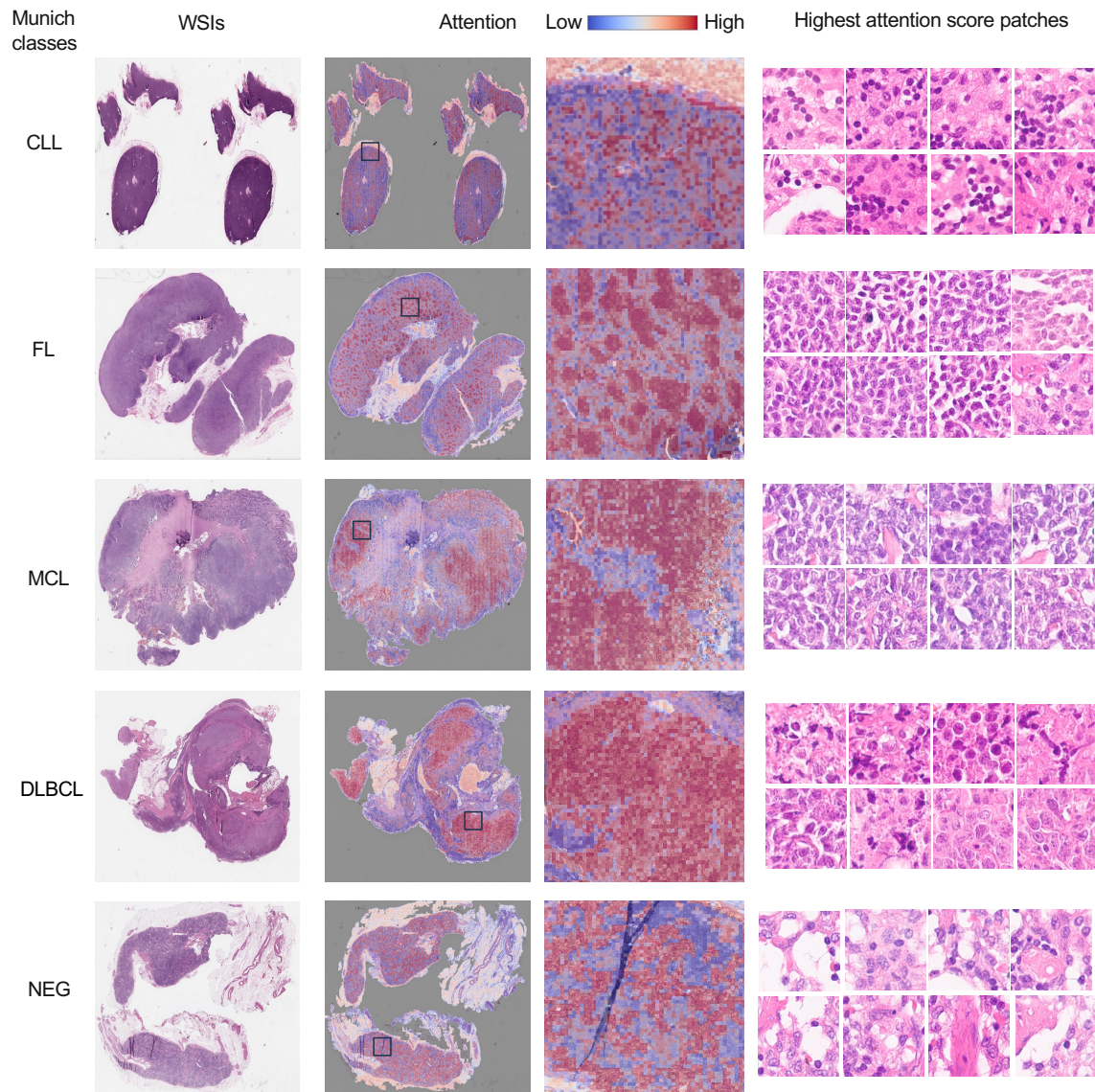


Figure 5: Attention visualization on IID Munich testset. Highest attention regions correspond to morphology, while lower attention regions mostly correspond to normal tissue or artifacts patches.

class imbalance, particularly for rare subtypes or limited-control classes, which may bias model training and lead to overconfident predictions for majority classes.

5. Conclusion

We present the first multicenter lymphoma benchmarking dataset comprising 999 HE-stained whole slide images across four common lymphoma subtypes (CLL, FL, MCL, DL-

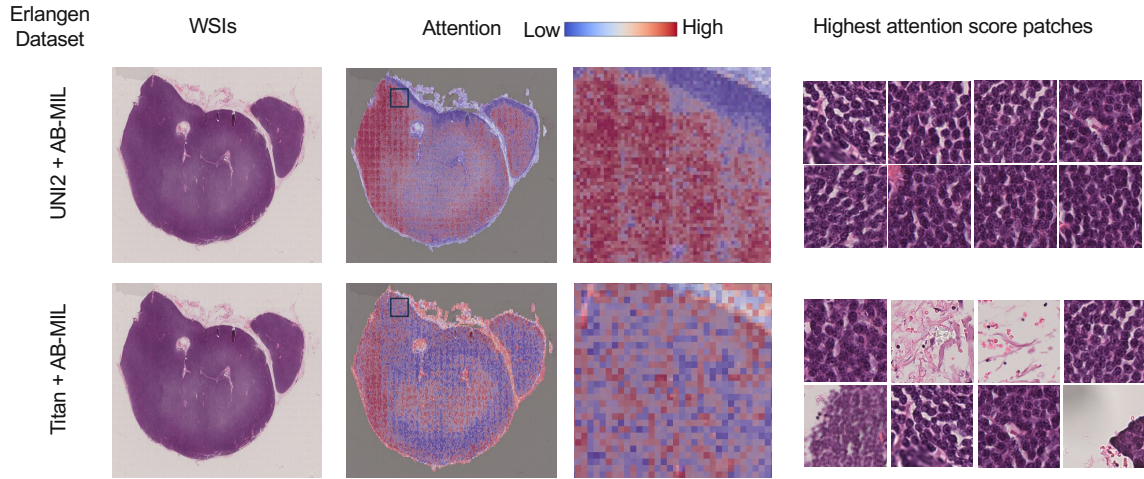


Figure 6: Attention visualization of CLL lymphoma subtype on OOD Erlangen cohort. UNI2 avoids artifact patches in the highest attention scores as compared to Titan.

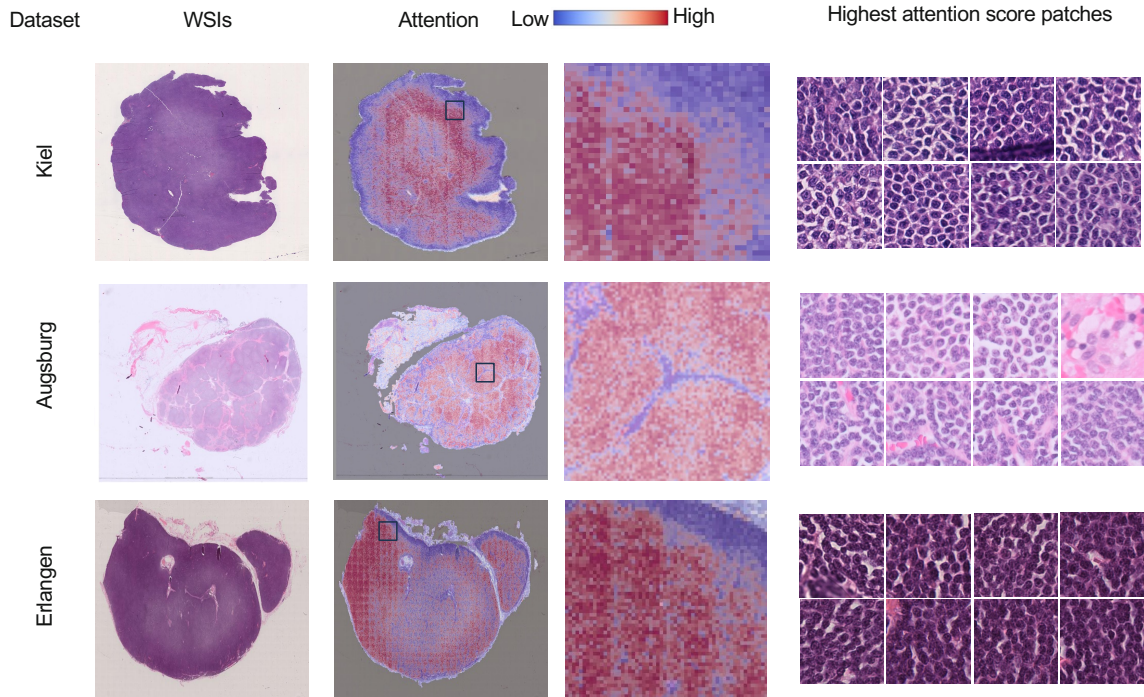


Figure 7: Attention visualization of CLL lymphoma subtype on OOD lymphoma testsets.

BCL) and healthy control tissue from four German centers. Combined with an automated multiple instance learning pipeline, we systematically evaluated five state-of-the-art pathology foundation models and two aggregation architectures across multiple magnifications.

Current “all-task” benchmark do not include lymphoma subtyping, and TCGA offers only a single lymphoma subtype (DLBCL) with limited histological diversity. In contrast, our multicenter benchmark focuses specifically on lymphoma, covering four common subtypes and healthy controls to enable a focused evaluation of this clinically important but so far underrepresented disease. On in-distribution test sets, all five foundation models (H-optimus-1, H0-mini, Virchow2, UNI2, Titan) achieved comparable performance with balanced accuracies exceeding 80%, demonstrating that current pathology foundation models have reached a similar level of representation quality for lymphoma subtyping. Both attention-based (AB-MIL) and transformer-based (TransMIL) aggregators performed similarly, with AB-MIL being computationally more efficient. Our magnification study revealed that $40\times$ resolution is sufficient for accurate classification, with no additional benefit from higher resolutions or cross-magnification aggregation strategies. Despite strong in-distribution performance, we observed substantial performance drops on out-of-distribution test sets (balanced accuracy around 60%), revealing significant generalization challenges. This degradation likely stems from scanner-specific color variations, site-specific staining protocols, and differences in patient populations across centers. In contrast to expensive and time-consuming IHC staining, flow cytometry, and molecular genetic tests, our approach demonstrates that inexpensive HE-stained WSIs can accurately determine common lymphoma subtypes when evaluated within the same clinical environment. An AI-augmented pathology workflow could guide initial screening to prioritize cases requiring expert review, potentially reducing turnaround times and allowing more efficient use of specialized diagnostic tests.

To advance lymphoma diagnostics toward clinical utility, larger multicenter studies with standardized protocols are essential. Future work should expand coverage to include rare lymphoma subtypes, incorporate stain normalization or domain adaptation techniques to improve cross-site generalization, and conduct prospective clinical validation studies. Integrating complementary modalities such as immunophenotyping data or clinical parameters may further enhance diagnostic accuracy. Ultimately, such systems could assist pathologists in maximizing diagnostic yield from HE-stained sections while minimizing the number of auxiliary tests required for accurate diagnosis.

Acknowledgments

C.M. acknowledges funding from the European Research Council (ERC) under the European Union’s Horizon 2020 research and innovation program (Grant Agreement No. 866411 & 101113551 & 101213822) and support from the Hightech Agenda Bayern.

Ethics statement

All experiments are conducted in accordance with the Declaration of Helsinki. The Technical University Munich (TUM) Ethics Committee approved the retrospective analysis of lymphoma data (Approval No. 79/20 S-KH).

Code availability statement

Our paper codes will be publicly available at <https://github.com/RaoUmer/LymphomaMIL>.

References

Rohan Bareja, Francisco Carrillo-Perez, Yuanning Zheng, Marija Pizurica, Tarak Nath Nandi, Jeanne Shen, Ravi Madduri, and Olivier Gevaert. Evaluating vision and pathology foundation models for computational pathology: A comprehensive benchmark study. *medRxiv*, pages 2025–05, 2025.

Bioptimus. H-optimus-1, 2025. URL <https://huggingface.co/bioptimus/H-optimus-1>.

Freddie Bray, Mathieu Laversanne, Elisabete Weiderpass, and Isabelle Soerjomataram. The ever-increasing importance of cancer as a leading cause of premature death worldwide. *Cancer*, 127(16):3029–3030, 2021.

Gabriele Campanella, Matthew G Hanna, Luke Geneslaw, Allen Miraflor, Vitor Werneck Krauss Silva, Klaus J Busam, Edi Brogi, Victor E Reuter, David S Klimstra, and Thomas J Fuchs. Clinical-grade computational pathology using weakly supervised deep learning on whole slide images. *Nature medicine*, 25(8):1301–1309, 2019.

Gabriele Campanella, Ricky Kwan, Eugene Fluder, Jennifer Zeng, Aryeh Stock, Brandon Veremis, Alexandros D Polydorides, Cyrus Hedvat, Adam Schoenfeld, Chad Vanderbilt, et al. Computational pathology at health system scale—self-supervised foundation models from three billion images. *arXiv preprint arXiv:2310.07033*, 2023.

Richard J Chen, Tong Ding, Ming Y Lu, Drew FK Williamson, Guillaume Jaume, Bowen Chen, Andrew Zhang, Daniel Shao, Andrew H Song, Muhammad Shaban, et al. Towards a general-purpose foundation model for computational pathology. *Nature Medicine*, 2024a.

Richard J Chen, Tong Ding, Ming Y Lu, Drew FK Williamson, Guillaume Jaume, Andrew H Song, Bowen Chen, Andrew Zhang, Daniel Shao, Muhammad Shaban, et al. Towards a general-purpose foundation model for computational pathology. *Nature Medicine*, 30(3):850–862, 2024b.

Tong Ding, Sophia J Wagner, Andrew H Song, Richard J Chen, Ming Y Lu, Andrew Zhang, Anurag J Vaidya, Guillaume Jaume, Muhammad Shaban, Ahrong Kim, et al. A multimodal whole-slide foundation model for pathology. *Nature Medicine*, pages 1–13, 2025.

Alexandre Filiot, Nicolas Dop, Oussama Tchita, Auriane Riou, Rémy Dubois, Thomas Peeters, Daria Valter, Marin Scalbert, Charlie Saillard, Geneviève Robin, et al. Distilling foundation models for robust and efficient models in digital pathology. In *International Conference on Medical Image Computing and Computer-Assisted Intervention*, pages 162–172. Springer, 2025.

Paolo Ghia, Andrés JM Ferreri, and Federico Caligaris-Cappio. Chronic lymphocytic leukemia. *Critical reviews in oncology/hematology*, 64(3):234–246, 2007.

Kaiming He, Xiangyu Zhang, Shaoqing Ren, and Jian Sun. Deep residual learning for image recognition. In *Proceedings of the IEEE conference on computer vision and pattern recognition*, pages 770–778, 2016.

Maximilian Ilse, Jakub M Tomczak, and Max Welling. Attention-based deep multiple instance learning. In *International conference on machine learning*, pages 2127–2136. PMLR, 2018.

William D Lewis, Seth Lilly, and Kristin L Jones. Lymphoma: diagnosis and treatment. *American family physician*, 101(1):34–41, 2020.

Lindsay M Morton, Sophia S Wang, Susan S Devesa, Patricia Hartge, Dennis D Weisenburger, and Martha S Linet. Lymphoma incidence patterns by who subtype in the united states, 1992-2001. *Blood*, 107(1):265–276, 2006.

Nikita Orlov, Wayne Chen, David Eckley, Tomasz Macura, Lior Shamir, Elaine Jaffe, and Ilya Goldberg. Automatic classification of lymphoma images with transform-based global features. *IEEE transactions on information technology in biomedicine : a publication of the IEEE Engineering in Medicine and Biology Society*, 14:1003–13, 07 2010. doi: 10.1109/TITB.2010.2050695.

Ario Sadafi, Asya Makhro, Anna Bogdanova, Nassir Navab, Tingying Peng, Shadi Albarqouni, and Carsten Marr. Attention based multiple instance learning for classification of blood cell disorders. In *International Conference on Medical Image Computing and Computer-Assisted Intervention*, pages 246–256. Springer, 2020.

Michael Schieber, Leo I Gordon, and Reem Karmali. Current overview and treatment of mantle cell lymphoma. *F1000Research*, 7:F1000–Faculty, 2018.

Daniel Sens, Ario Sadafi, Francesco Paolo Casale, Nassir Navab, and Carsten Marr. Bel: A bag embedding loss for transformer enhances multiple instance whole slide image classification. In *2023 IEEE 20th International Symposium on Biomedical Imaging (ISBI)*, pages 1–5. IEEE, 2023.

Zhuchen Shao, Hao Bian, Yang Chen, Yifeng Wang, Jian Zhang, Xiangyang Ji, et al. Transmil: Transformer based correlated multiple instance learning for whole slide image classification. *Advances in Neural Information Processing Systems*, 34:2136–2147, 2021.

Eugene Vorontsov, Alican Bozkurt, Adam Casson, George Shaikovski, Michal Zelechowski, Kristen Severson, Eric Zimmermann, James Hall, Neil Tenenholtz, Nicolo Fusi, et al. A foundation model for clinical-grade computational pathology and rare cancers detection. *Nature medicine*, 30(10):2924–2935, 2024.

Damir Vrabc, Akshay Smit, Rebecca Rojansky, Yasodha Natkunam, Ranjana H Advani, Andrew Y Ng, Sebastian Fernandez-Pol, and Pranav Rajpurkar. Dlbcl-morph: Morphological features computed using deep learning for an annotated digital dlbcl image set. *Scientific Data*, 8(1):135, 2021.

Luc Xerri, Stephan Dirnhofer, Leticia Quintanilla-Martinez, Birgitta Sander, John KC Chan, Elias Campo, Steven H Swerdlow, and German Ott. The heterogeneity of follicular lymphomas: from early development to transformation. *Virchows Archiv*, 468(2): 127–139, 2016.

Andrew Zhang, Guillaume Jaume, Anurag Vaidya, Tong Ding, and Faisal Mahmood. Accelerating data processing and benchmarking of ai models for pathology. *arXiv preprint arXiv:2502.06750*, 2025.

Eric Zimmermann, Eugene Vorontsov, Julian Viret, Adam Casson, Michal Zelechowski, George Shaikovski, Neil Tenenholtz, James Hall, Thomas Fuchs, Nicolo Fusi, Siqi Liu, and Kristen Severson. Virchow2: Scaling self-supervised mixed magnification models in pathology. *arXiv preprint arXiv:2408.00738*, 2024.